Electronic Supplementary Material (ESI) for Catalysis Science & Technology.

Electronic Supplementary Information

C-C coupling at a zeolite-supported Rh(I) complex. DFT search for the mechanism

Sai V. C. Vummaleti,[a] Nishamol Kuriakose,[a] Shrabani Dinda,[§,a] Yin Wu,[a,b]
Alexander Genest,[a] Notker Rösch*[,a,b]

[a] Institute of High Performance Computing, Agency for Science, Technology and Research, 1 Fusionopolis Way, #16-6 Connexis, Singapore 138632

[b] Department Chemie and Catalysis Research Center, Technische Universität München, 85747 Garching, Germany, *E-mail: roesch@mytum.de

[§] Present address: CSIR-Indian Institute of Chemical Technology, Uppal Road, Tarnaka, Hyderabad 500007, India

* Corresponding author. E-mail: roesch@mytum.de

Section S1. Zeolite models

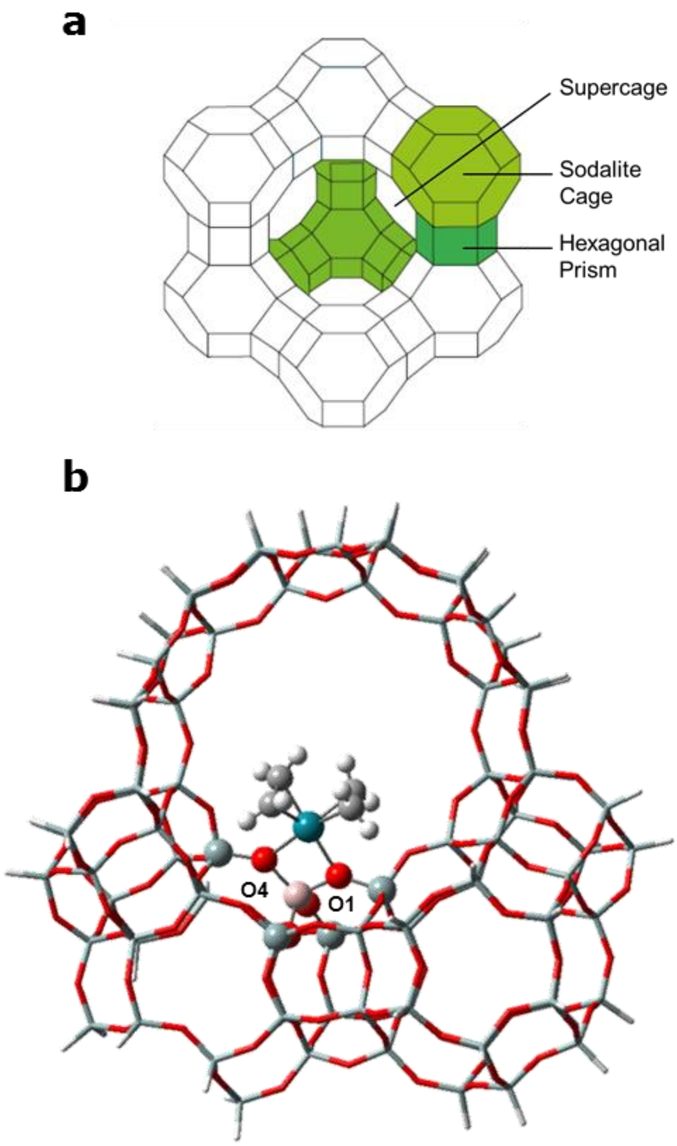

Figure S1. (a) Schematic representation of the structure of faujasite and its three building blocks. (b) The 5/83T cluster model with the extra framework fragment $[Rh(C_2H_4)_2]^+$ anchored at the centers O1 and O4 of the supercage. The (high-level) QM partition is rendered in ball-and-stick fashion, bonds in the (low-level) MM partition are shown as sticks only.

Section S2. Alternative pathway to ethane starting from complex 4

Hydrogenation of the second ethene in complex **4**, $[Rh(C_2H_4)(C_2H_5)(H)]^+$, leads to the Rh-diethyl complex **17**, $[Rh(C_2H_5)_2]^+$. This reaction is thermoneutral, essentially without a barrier, G_a(**4→17**) = 1 kJ mol^{-1}, Scheme S1. Coordination of a second H_2 molecule to the Rh center in complex **17** is slightly endergonic and yields complex **18**, $[Rh(C_2H_5)_2(H_2)]^+$, G_r(**17→18**) = 19 kJ mol^{-1}, Scheme S1. Complex **18** exhibits a pseudo trigonal bipyramidal geometry with the H_2 molecule coordinated in the axial position, Figure S8. Structure **19** is an isomer of complex **18**, where H_2 is rearranged to an equatorial position at the metal center; it is calculated 25 kJ mol^{-1} lower in energy, G_r(**18→19**) = -25 kJ mol^{-1}, Scheme S1. Next, the hydrogenation of one of the two ethyl ligands in **19** yields ethane coordinated to the Rh, complex **20**, $[Rh(C_2H_6)(C_2H_5)(H)]^+$. This step is exergonic, G_r(**19→20**) = -9 kJ mol^{-1}, requiring to overcome a small activation barrier, G_r(**19→20**) = 7 kJ mol^{-1}, Scheme S1. The hydrogenation of the second ethyl ligand yields complex **21**, $[Rh(C_2H_6)_2]^+$, coordinating two ethane molecules at the Rh metal center. This highly endothermic step, G_r(**20→21**) = 62 kJ mol^{-1}, features a moderate free energy barrier, G_a(**20→21**) = 70 kJ mol^{-1}, Scheme S1.

Complex **1** can be regenerated from complex **21** by the sequential coordination of two units of ethene at the metal center, with the simultaneous release of two ethane molecules. These steps are highly exergonic, G_r(**21→22**) = -123 kJ mol^{-1}, and G_r(**22→23**) = -119 kJ mol^{-1}, Scheme S1. The release of ethane into the gas-phase is exergonic, G_r(**23→6**) = -15 kJ mol^{-1}. Thus, complex **23** connects to the ethene hydrogenation pathway described in Scheme 3 of the main text, to regenerate **1** via **6→1**, Scheme S1. Overall, this alternative pathway to the hydrogenation of ethene is unlikely to occur because the TS **20→21** of ethane formation lies 62 kJ mol^{-1} above **1**. This barrier is 40 kJ mol^{-1} higher in absolute terms than the analogous TS **4-5**, 22 kJ mol^{-1} above **1**, Scheme 3 of the main text and Figure S2.

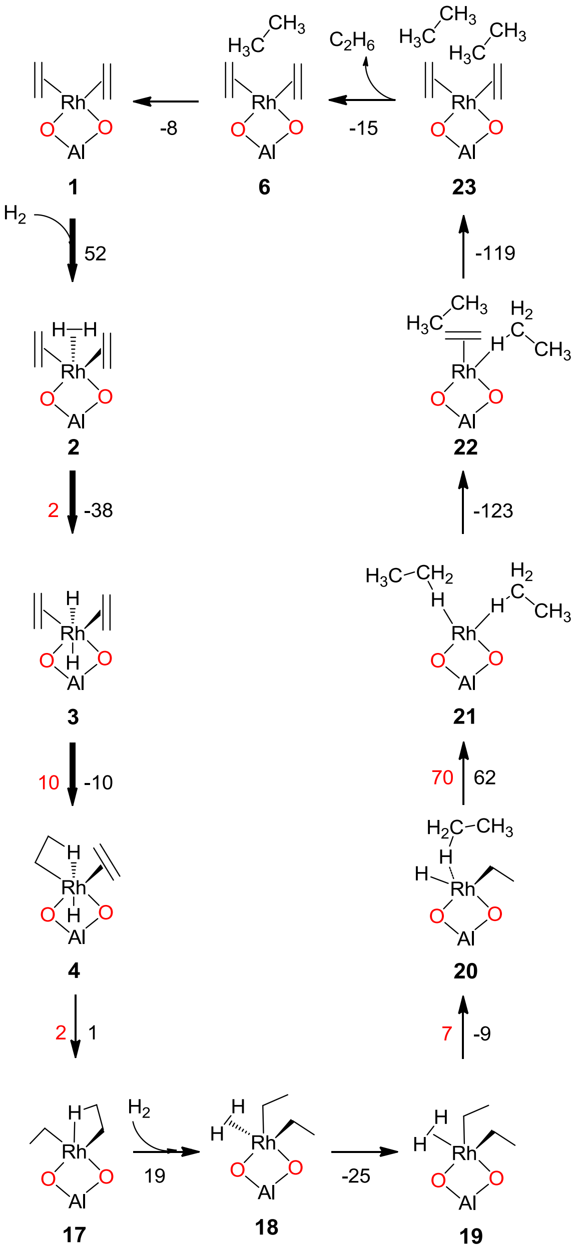

Scheme S1. Reaction network of an alternative ethene hydrogenation path starting from complex **4** for the zeolite-supported 2-ligand Rh(I) complex **1**, $[Rh(C_2H_4)_2]^+$. Reaction and activation free energies, in kJ mol^{-1}, of individual steps are given as black and red values, respectively. Bold black arrows mark the steps leading to complex **4**.

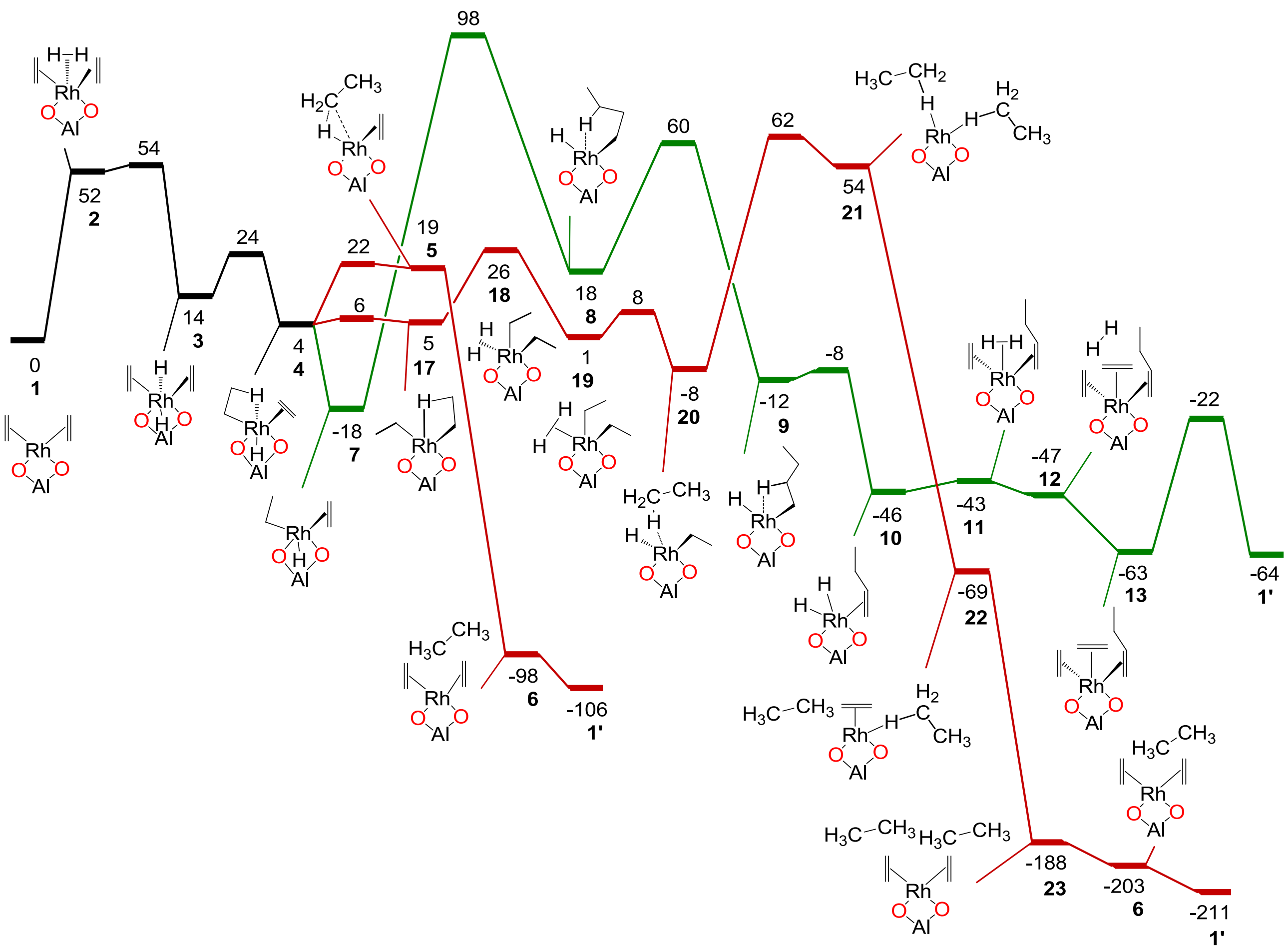

Figure S2. Complete free energy profile for the hydrogenation and the dimerization of ethene via the pathway **CA1** at a 2-ligand Rh(I) complex. Free energies, in kJ mol^{-1}, with respect to complex **1** and H_2 as well as C_2H_4 in the gas phase, at infinite separation. Intermediates are labeled and shown in sketches. Color coding according to the product: red – ethane; green – butene; black – joint section of the pathways.

Table S1. Total energies (au) of reactants, transition states, and products for the reaction network of ethene hydrogenation shown in Scheme 2 of the main text. Relative reaction free energies ΔG_{rel} (kJ mol^{-1}) with respect to the corresponding preceding intermediate, and absolute reaction free energies ΔG_{abs} (kJ mol^{-1}) with respect to complex **1,** $[Rh(C_2H_4)_2]^+$.

Complex	Total Energy	ΔG_{abs}	ΔG_{rel}
Ethylene	-78.46632		
H_2	-1.16742		
Ethane	-79.67395		
Butene	-156.95680		
1	-1971.07049	0	0
2	-1972.21807	52	52
2-3	-1972.21724	54	2
3	-1972.23243	14	-38
3-4	-1972.22868	24	10
4	-1972.23645	4	-10
4-5	-1972.22934	22	18
5	-1972.23060	19	15
6	-2050.74138	-98	-117
7	-1972.24459	-18	-22
7-8	-1972.20064	98	116
8	-1972.23114	18	36
8-9	-1972.21498	60	42
9	-1972.24236	-12	-30
9-10	-1972.24389	-8	4
10	-1972.25535	-46	-34
11	-2050.72045	-43	3
12	-2129.18855	-47	-4
13	-2128.02715	-63	-16
13-1	-2128.01137	-22	41
1-14	-1971.01779	138	138
14	-2128.02715	106	106
2-15	-1972.18122	149	97
15	-1972.21915	101	49
3-16	-1972.17529	164	150
16	-1972.22694	43	29
4_17	-1972.23566	6	2
17	-1972.23528	5	1
18	-1973.39535	26	19
19	-1973.40494	1	-25
19_20	-1973.40217	8	7
20	-1973.40843	-8	-9
20_21	-1973.38183	62	70
21	-1973.38490	54	62
22	-2051.89786	-69	-123
23	-2130.40963	-188	-119

Section S3. Bifunctional mechanism

First we describe the models constructed for probing the experimentally suggested bifunctional mechanism,[1, 2] where the Al-OH centers at the zeolite wall take up a supporting role, "activating" a second ethene moiety for the C–C coupling step between two ethene species, see Scheme S2 as well as Figures S3 and S4. The C–C coupling reaction energetics with the constructed models is shown in Table S2.

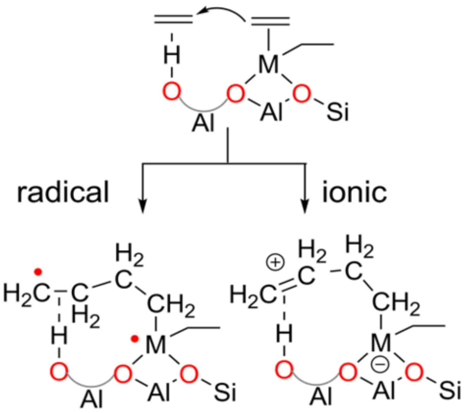

Scheme S2. Proposed bifunctional route to C–C coupling in a zeolite cavity with Rh(I) complex **1**, $[Rh(C_2H_4)_2]^+$, where an ethene ligand of the supported metal complex interacts with a second ethene species adsorbed at a nearby Al–OH site, giving rise to a zwitterionic or a radical variant.

Models. Following the proposition in the experiment work,[1, 2] we used extended QM partitions, always comprising 11 T atoms of the basic 83T cluster, to accommodate the second Al-OH moiety. We applied three constraints to the relative arrangement of the two Al centers. (*i*) The second Al center cannot be located too far from the Rh center as the two carbon centers, one on each of the two ethene molecules at two Al sites, have to come sufficiently close to each other to interact for forming the new C–C bond. (*ii*) Yet, direct Al–O–Al sequences are not permitted in a zeolite framework according to Loewenstein's rule.[3] Thus, honoring both these constraints, we considered zeolite models entailing sequences of the type Al–O–(Si–O)$_n$–Al, n = 1–3. In experiment, the existence of such sequences primarily depends on the conditions of the zeolite synthesis.[4] These sequences are fully covered in the extended QM partition. (*iii*) We probed only rotational variants, of the Rh complex and the ethylene adsorbed on the Al–OH moiety, which showed a relative orientation favorable for C–C coupling.

We constructed two types of 11/83T models of faujasite, labeled **A** and **B**, considering promising locations of the second Al center. In models **A**, the sequences Al–O–(Si–O)$_n$–Al, n = 1–3, are part of a single 12-MR, Figures S3 A and S4. In models **B**, the second Al center is placed outside the 12-MR that carries the Rh complex, in a 4 T ring, Figure S3 B. Models **B** are restricted to Al–O–Si–O–Al chains, i.e., to n = 1, because longer chains, n = 2, 3, do not admit

C–C bond formation. Therefore, in models **B**, the QM partition is selected to comprise one 6-MR and three 4-MR units, Figures S3 B and S4. We also checked other plausible positions of the second Al center in the vicinity of the Rh center. However, none of them fulfilled condition (*i*) discussed above, namely that the second Al center cannot be too far from the first one.

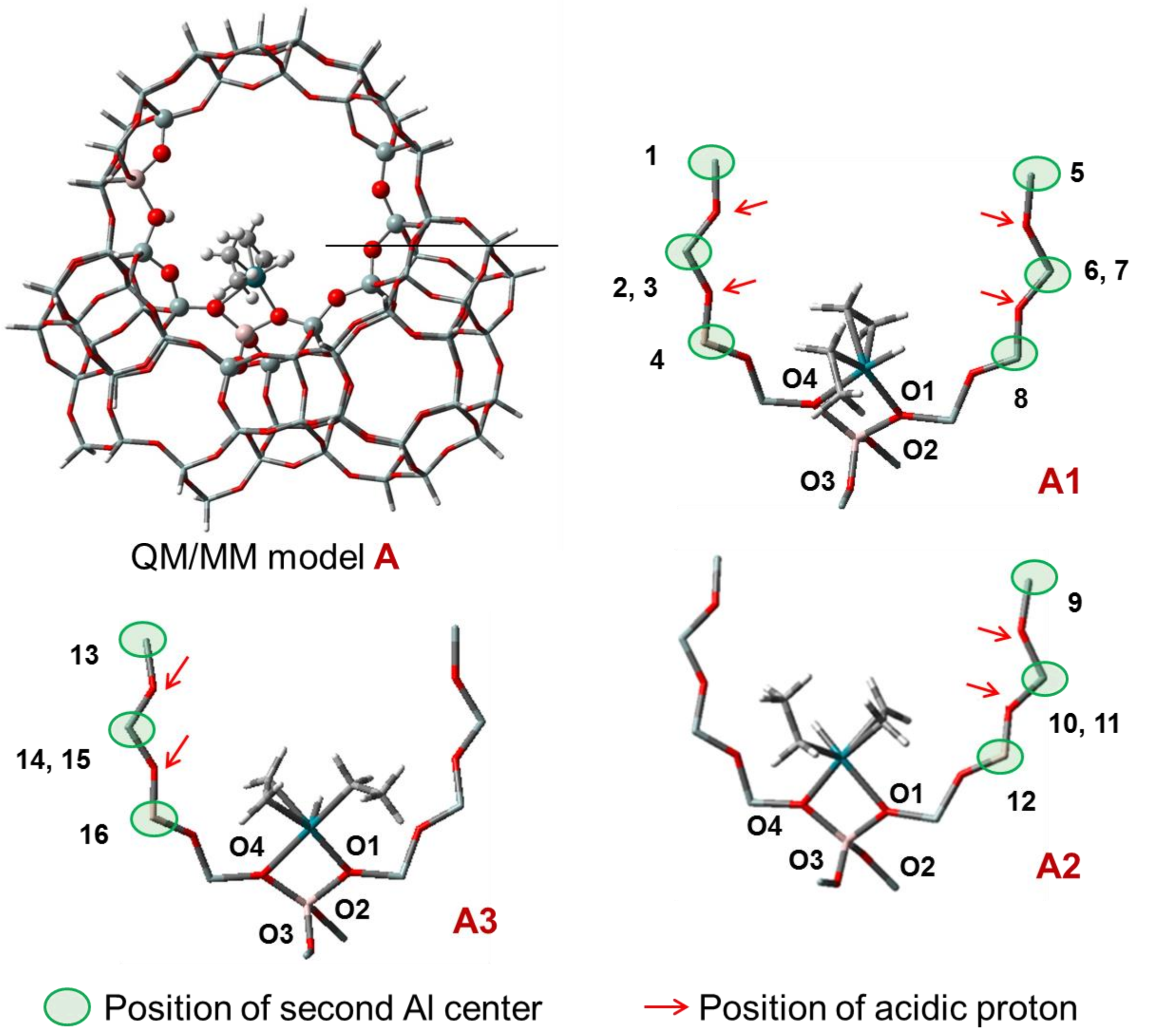

Figure S3 A. Variant **A** of the QM/MM embedding 11/83T models: ligand configurations **A1**, **A2**, and **A3** of the central Rh moiety in combination with various locations of the second Al-OH moiety, carrying an acidic proton and a second ethene molecule. Values n discriminate the unique structures **A.n**, n = 1–16; see Figure S3. For clarity, the 11T QM partition of the 11/83T cluster is shown for a single ligand orientation only at the Rh fragment. Two neighboring labels indicate positions where two possibilities exist for placing the proton.

Our preceding study[5] on the selective hydrogenation process revealed that complex **4**, $[Rh(C_2H_4)(C_2H_5)(H)]^+$, adsorbed at the 12-MR of the supercage, is an important complex, in agreement with experiment.[1,2] For this complex **4**, we constructed the initial configurations **Am**, m =1–3, using the 11/83T QM/MM model **A**, Figures S2, S3. In configuration **A1**, the hydride is placed *trans* to the O4 center. The metal fragment of configuration **A2** retains a distorted square-pyramidal geometry where the hydride is *trans* to the O1 center and ethyl is oriented *trans* to the O4 moiety. In contrast, the ethene ligand of the Rh center in configuration **A3** is pointing to the opposite side of the supercage ring, where we also placed the remaining ethene at an Al–OH moiety, Figures S3 A and S4. However during the TS search, the ligand configuration of all **A3** complexes rearranged to the one of the corresponding **A1** congener. For successful C–C coupling, the ethene molecule, coordinated at the Al–OH moiety, has to reside on the same side as the metal-coordinated ethene, Figures S3 A and S4. The various locations of the second Al center for each ligand arrangement resulted in 12 variants of the initial state structures which we enumerate as **A.n**, n = 1–12, Figure S3 A.

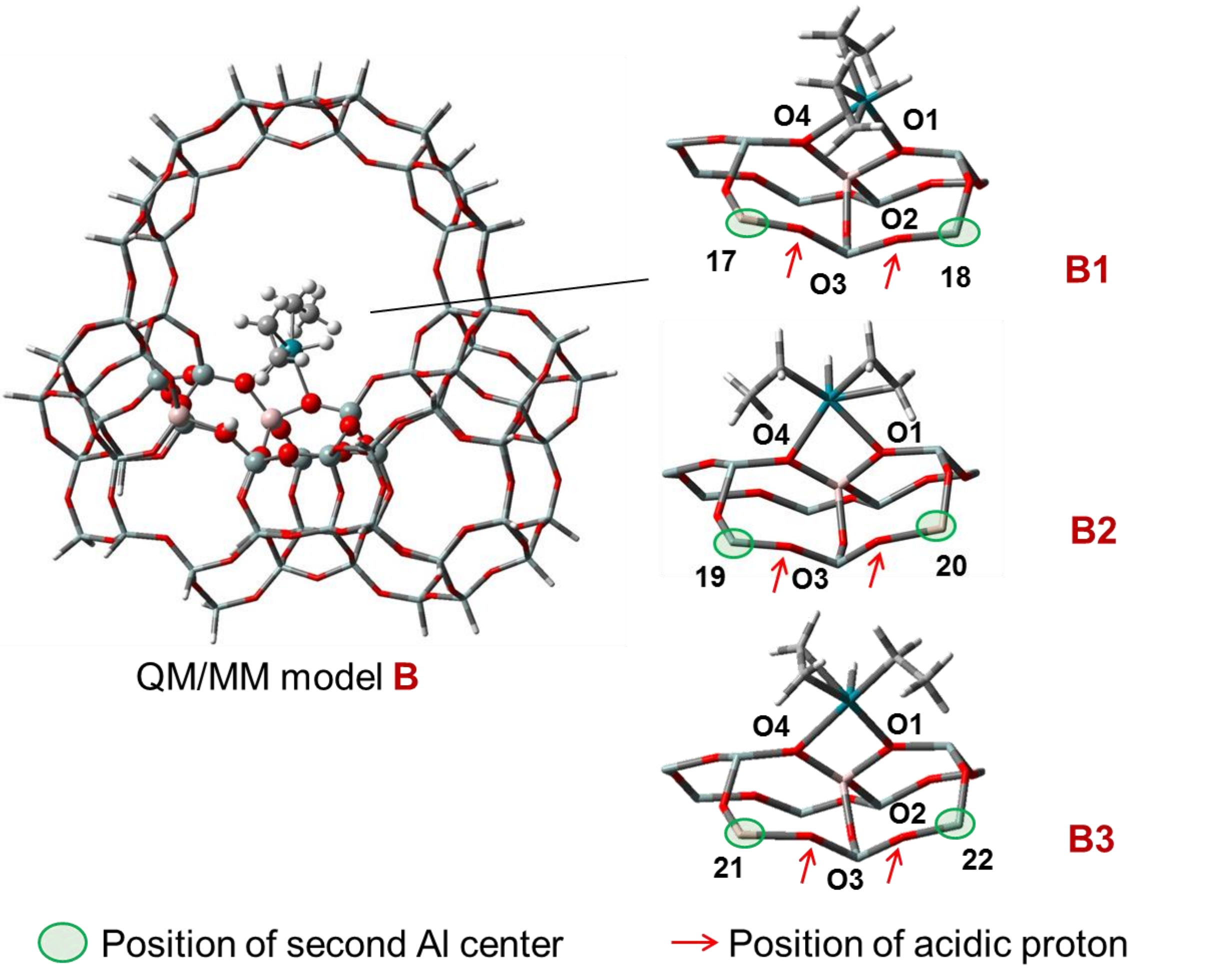

Figure S3 B. Variant **B** of the QM/MM embedding 11/83T models: ligand configurations **B1**, **B2**, and **B3** of the central Rh moiety in combination with various locations of the second Al-OH moiety, carrying an acidic proton and a second ethene molecule. Values n discriminate the unique structures **B.n**, n = 17–22; see Figure S3. For clarity, the 11T QM partition of the 11/83T cluster is shown for a single ligand orientation only at the Rh fragment.

For models **B**, the configurations **Bm**, m = 1–3, of complex **4**, $[Rh(C_2H_4)(C_2H_5)(H)]^+$, exhibit similar initial ligand arrangements as the corresponding configurations **Am**. For each ligand orientation **Bm**, we considered two locations of the second Al center. A rotation of the

Rh moieties in configurations **B2** and **B3** renders the relative orientation and the distance between the two pertinent ethene species the same as in the resulting two final structures of **B1**, **B.17** and **B.18**, Figures S3 B and S4. Therefore, after optimization of the initial structures, we were left with only these two configurations.

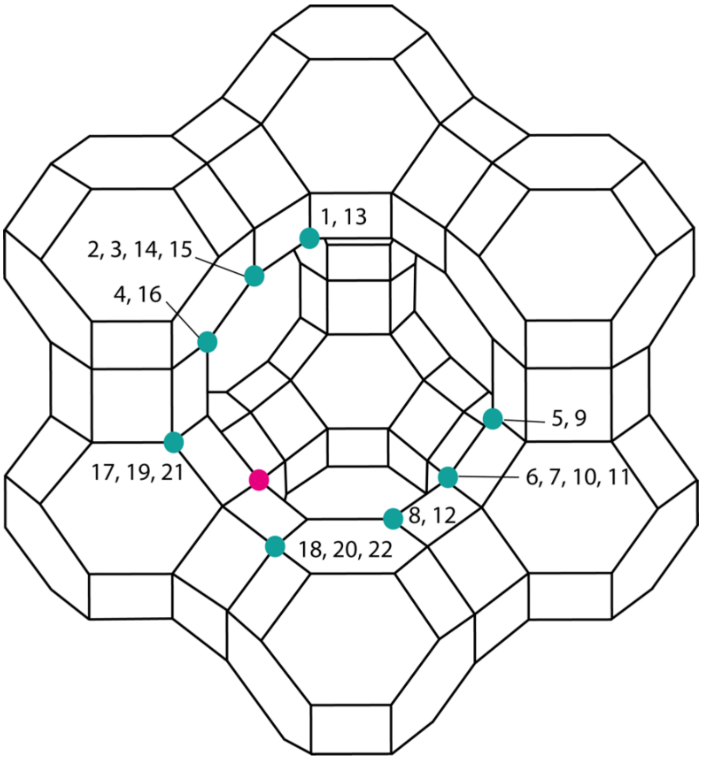

Figure S4. Positions of the second Al center (cyan) in variants **A** and **B** of the QM/MM embedding, relative to the first Al center (red). Values n identify 22 unique configurations **A.n**, n = 1–16, inside the sodalite cage, and **B.n**, n = 17–22, outside the sodalite cage.

C–C coupling reaction energetics. For the bifunctional mechanism, following the experiment,[1] we selected only situations where external hydrogen is prevented from being incorporated into the product. This is a severe limitation which even prevents the proton of the Al–OH moiety to be incorporated in the product butene. After all, if used, that proton would have to be replenished from the feed. In other words, the proton close to the second Al center will only help to bind the (second) ethene at the zeolite wall. The result of the isotope experiment also excludes the insertion of any hydride ligand at the Rh center into the product.[1]

Table S2 lists the variants that were determined to yield stable products in the triplet state. As can be seen, we were left with only 11 complexes representing successful C–C coupling steps, Table S2. Additionally, we were able to determine only radical products in the triplet state, but failed to identify any stable zwitterionic product, Figure S5 of the ESI. The energies of those radicals relative to the preceding intermediate fall in a relatively narrow range, from 129 kJ mol^{-1} to 153 kJ mol^{-1} (Table S2 of the ESI), as expected for triplet states of hydrocarbon moieties without stabilizing functional groups. The products at the lower end of this energy range were obtained from intermediates **A.4** and **B.17**, where the two organic moieties to be bonded are oriented toward the same side of the Rh complex; the Al centers of both intermediates are separated by the shortest chain possible, Al–O–Si–O–Al. The lowest-energy product formed at the opposite site of the Rh complex, with a reaction energy of 136 kJ mol^{-1}, is obtained from the intermediate **A.10** where the two active sites are further separated, by Al–O–(Si–O)$_n$–Al, n = 2.

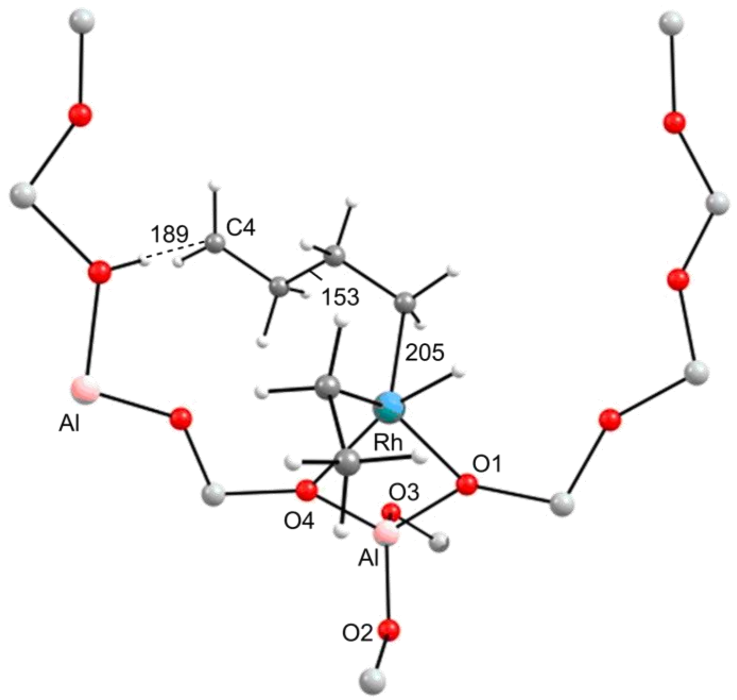

Figure S5. Optimized structure of the C–C coupled product, a Rh–butyl radical, model variant **A.4**. A Mulliken analysis of the triplet radical revealed that the spin density is localized at the Rh center (79%) and the terminal carbon atom C4 of the hydrocarbon (90%). Only the 11T QM partition of the 11/83T cluster model is shown. Selected distances in pm.

Table S2. Reaction free reaction energies ΔG_r (kJ mol^{-1}) of the C–C coupling step for reaching the triplet product of selected model variants (Figures S3 and S4) of the bifunctional mechanism.

Configurations	**Variant**[a]	ΔG_r
A1	**A.1**	143
	A.2	138
	A.3	144
	A.4	129
	A.6	153
A2	**A.9**	142
	A.10	136
	A.11	147
	A.12	144
B1	**B.17**	129
	B.18	142

[a] The product could not be located for the initial structures **A.5**, **A.7**, and **A.8**.

Section S4. Alternative routes of the CA2 pathway

A glance at Scheme 4 of the main text reveals that the catalytic cycle **7** → **8** → **9** → **10** → **11** → **7** does not represent the complete story, as there are alternative routes, leading to side products, e.g., ethane and butane. In particular, it is important to evaluate pathways that might lead to ethene hydrogenation. Figure S6 provides an energy profile including all side reactions depicted in Scheme 4. In the following, we are discussing these alternatives in increasing order of the labels designating the intermediates where these alternative pathways are branching off.

Intermediate **26** can be converted to two other intermediates, besides the preferred pathway leading to complex **27**, Scheme 4 of the main text and Figure S2. In view of the low barrier G_a(**26**→**27**) = 4 kJ mol^{-1} we do not expect any of these alternatives to play a role in a direct comparison. The pathway to C–C coupling, **26**→**44**, is unlikely to occur due to the associated high free energy barrier of ~100 kJ mol^{-1}, Scheme 4 of the main text and Figure S2. Next, the transfer of a H atom to the metal center in **26** leads to the Rh–H complex **32**, $[Rh(C_2H_4)_2(C_2H_5)(H)]^+$. This step is exergonic, G_r(**26**→**32**) = -18 kJ mol^{-1}, over a moderate barrier G_a(**26**→**32**) = 36 kJ mol^{-1}, Scheme 4 of the main text and Figure S2. The TS **26-32**, crucial for ethane formation, is 32 kJ mol^{-1} higher in energy, G_a(**26**→**32**) = 36 kJ mol^{-1}, than TS **26-27** leading to the stable Rh-diethyl complex **27**, G_a(**26**→**27**) = 4 kJ mol^{-1}, Scheme 4 of the main text and Figure S2. In addition, complex **27** is 15 kJ mol^{-1} more stable than **32**. Starting from **32**, one may also generate a butyl ligand in structure **53**, but via quite high a barrier, G_a(**16**→**18**) = 125 kJ mol^{-1}.

C–C coupling in **27** between the two ethyl moieties to yield butane as side product is by 14 kJ mol^{-1} less facile, G_a(**27**→**45**) = 119 kJ mol^{-1}, than the preferred reaction **27**→**28**. Addition of another ethene to **27** resulting in complex **47**, after an endothermic transformation, may be followed by a C–C coupling reaction, **47**→**29**, that yields the stable butyl complex **29**. However, this path to **29** exhibits an extremely high-lying TS, G_a(**27**→**47**→**29**) = 149 kJ mol^{-1}, in comparison to G_a(**27**→**28**) = 103 kJ mol^{-1}, both values with respect to **27**, Scheme 4 of the main text and Figure S2. Finally, coordination of an additional molecule of H_2 to **27** is calculated to be endergonic, G_r(**27**→**48**) = 43 kJ mol^{-1}. The subsequent reaction from **48** yields the ethane coordinated product complex **49**. This step is exergonic, G_r(**48**→**49**) = -20 kJ mol^{-1}, over a moderate barrier G_a(**48**→**49**) = 37 kJ mol^{-1}, Scheme 4 of the main text and Figure S2.

Besides the concerted step **29**→**30** discussed in the main text, the butyl group of complex **29** can also be transformed to a butene via the stepwise process **29**→**41**→**30**, Scheme 4 of the main text and Figure S2. The intermediate Rh–H complex **41** is reached via a free energy barrier G_a(**29**→**41**) = 13 kJ mol^{-1}, which is higher in energy by 10 kJ mol^{-1} then the calculated barrier for the reaction **29**→**30**. Additionally, the subsequent hydrogenation of a nearby ethene ligand requires overcoming a free energy barrier that is about twice as high, G_a(**41→30**) = 27 kJ mol^{-1}. The alternative path to ethane via complex **41** is kinetically hindered because its TS is 40 kJ mol^{-1} higher, G_a(**29→50**) = 43 kJ mol^{-1}, than the main path, G_a(**29→30**) = 3 kJ mol^{-1}, Scheme 4 of the main text and Figure S2.

Section S5. Overview of the CA2 pathway

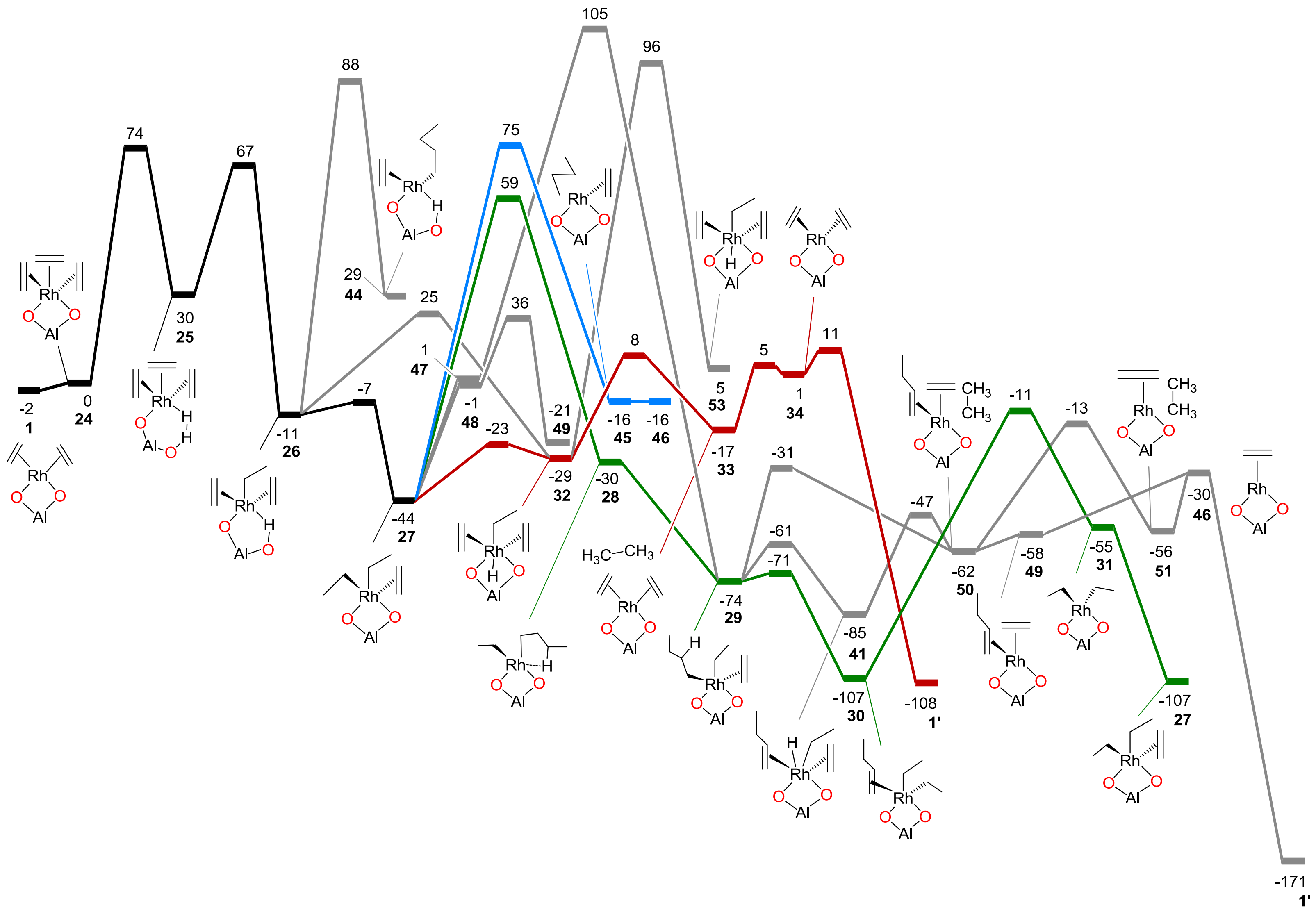

Figure S6. Complete free energy profile for ethene hydrogenation and dimerization via the pathway **CA2** at a 3-ligand Rh(I) complex. Free energies (kJ mol^{-1}) with respect to complex **24** as well as H_2 and C_2H_4 in the gas phase, at infinite separation. Intermediates are labeled and shown in sketches. Color coding according to the product: red – ethane; green – butene; blue – butane; grey – variants; black – joint section of the pathways.

Section S6. Alternative routes of the MC2 and MC3 pathways

Scheme 5 of the main text reveals that complex **37**, $[Rh(C_2H_4)(H)(C_4H_9)]^+$, interconnects pathways **MC2** and **CA2** via **37→54→55→29**. Complex **37** carries the ligands ethene and H in a *trans* arrangement relative to the Rh center, Figure S4. A *cis* rearrangement of the ethene ligand and the H atom is required for transferring the hydrogen to the ethene in a facile fashion. This rearrangement occurs via the insertion of an H atom into the $Rh–O_1$ bond of the zeolite framework, forming complex **54**, thereby generating the bridge Rh–H–O1 with Rh–H = 195 pm, O1–H = 108 pm, Scheme 5 of the main text and Figure S8. This insertion step is notably exergonic, G_r(**37→54**) = -65 kJ mol^{-1}, and proceeds via the barrier G_a(**37→54**) = 58 kJ mol^{-1}. However, this pathway is unlikely as the latter TS **37-54** is 33 kJ mol^{-1} higher in energy than TS **37-38** leading to the stable rotamer complex **38**, G_a(**37→38**) = 25 kJ mol^{-1}, Scheme 5 of the main text and Figure S8. The next step is the facile hydrogenation of the ethene ligand of **54** leading to complex **55**, $[Rh(C_2H_5)(C_4H_9)]^+$, G_r(**54→55**) = 2 kJ mol^{-1}, G_a(**54→55**) = 27 kJ mol^{-1}, Scheme 5 of the main text and Figure S8. Finally, the coordination of a further ethene moiety to the Rh center of structure **55** proceeds without a barrier and is exergonic, G_r(**55→29**) = -36 kJ mol^{-1}, forming complex **29,** $[Rh(C_2H_5)(C_4H_9)(C_2H_4)]^+$. Thus, complex **29** connects to the ethene dimerization **CA2** pathway described in Scheme 4 of the main text.

Section S7. Overview of the MC2 and MC3 pathways

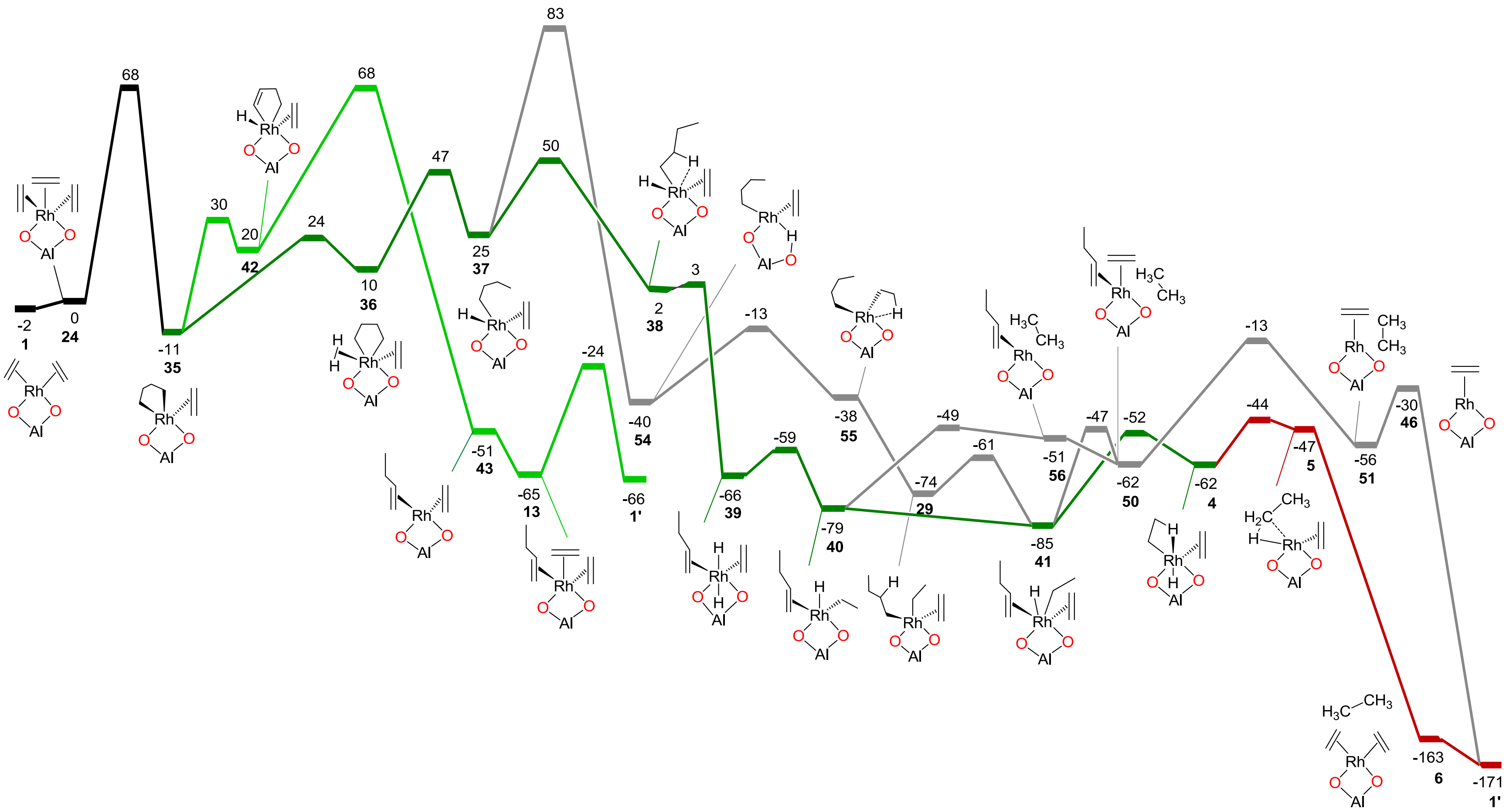

Figure S7. Complete free energy profile for hydrogenation and dimerization of ethene via the pathways **MC2** and **MC3** at a 3-ligand Rh(I) complex. Free energies (kJ mol^{-1}) with respect to complex **24** as well as H_2 and C_2H_4 in the gas phase, at infinite separation. Intermediates are labeled and shown in sketches. Color coding according to the product: red – ethane; green – butene; grey – variants; black – joint section of the pathways. The pathway **MC3** is shown in light green.

Section S8. Free energies of reactants, intermediates, and products

Table S3. Total energies (au) of reactants, transition states, and products for the hydrogenation and dimerization of ethene, Schemes 3 and 4 of the main text. Relative reaction free energies ΔG_{rel} (kJ mol^{-1}) with respect to the respective preceding intermediate, and absolute reaction free energies ΔG_{abs} (kJ mol^{-1}) with respect to complex **24,** $[Rh(C_2H_4)_3]^+$.

Complex	Total Energy	ΔG_{abs}	ΔG_{rel}	Complex	Total Energy	ΔG_{abs}	ΔG_{rel}
Butane	-158.15944			**39-40**	-2050.72575	-59	7
24	-2049.53592	0	2	**40**	-2050.73346	-79	-13
24_25	-2050.67508	74	74	**29-41**	-2129.19305	-61	13
25	-2050.69176	30	30	**41**	-2129.20194	-85	-11
25_26	-2050.67772	67	37	**41-30**	-2129.19164	-58	27
26	-2050.70757	-11	-41	**41-50**	-2129.18761	-47	38
26_27	-2050.70613	-7	4	**41-4**	-2129.18949	-52	33
27	-2050.71996	-44	-33	**35_42**	-2049.52431	30	41
27_28	-2050.68070	59	103	**42**	-2049.52832	20	31
28	-2050.71478	-30	14	**42_43**	-2049.51007	68	48
29	-2129.19778	-74	-44	**43**	-2049.55550	-51	-71
29_30	-2129.19685	-71	3	**26_44**	-2050.66995	88	99
30	-2129.21024	-107	-33	**44**	-2050.69243	29	40
30_31	-2129.17395	-11	96	**27_45**	-2050.67468	75	119
31	-1972.23369	-55	52	**45**	-2050.70959	-16	28
30_27	-2207.61137	65	172	**46**	-1892.55009	-16	0
26_32	-2050.69385	25	36	**47**	-2129.16943	1	45
27_32	-2050.71223	-23	21	**47_29**	-2129.12959	105	104
32	-2050.71446	-29	-18	**48**	-2051.87094	-1	43
32-33	-2050.70031	8	37	**48_49**	-2051.85692	36	37
33	-2050.70995	-17	12	**49**	-2051.87886	-21	-20
33-34	-2050.70132	5	22	**29_50**	-2129.18162	-31	43
34	-1971.02888	1	18	**50**	-2129.19344	-62	12
34-1	-1971.02510	11	10	**50_51**	-2129.17451	-13	49
24-35	-2049.51003	68	68	**51**	-1972.23404	-56	6
35	-2049.53998	-11	-11	**52**	-2049.51763	-58	4
35-36	-2050.69437	24	35	**32_53**	-2050.66679	96	125
36	-2050.69955	10	21	**53**	-2050.70146	5	34
36-37	-2050.68532	47	37	**37_54**	-2050.67172	83	58
37	-2050.69396	25	15	**54**	-2050.71839	-40	-65
37-38	-2050.68428	50	25	**54_55**	-2050.70812	-13	27
38	-2050.70246	2	-23	**55**	-2050.71761	-38	2
38-39	-2050.70203	3	1	**40_56**	-2050.72203	-49	30
39	-2050.72859	-66	-68	**56**	-2050.72261	-51	28

Section S9. Extended QM/MM zeolite models and functionals B3LYP and M06

To evaluate the accuracy of the observed energy difference of 18 kJ mol^{-1} between the crucial barriers of variants **MC2** and **MC3**, Figure S7 and Figure 3 of the main text, we examined several variations in the size of the QM/MM zeolite models[6] (5/240T and 11/83T) and the energy functional (B3LYP[7-10] and M06[11]). To this end, we calculated the thermodynamic stability of six key structures, four intermediates (**24**, **35**, **37**, and **42**) and two transition states (TS **37→38** and TS **42→43**), Scheme 5 of the main text and Figure S7.

Models. We used the extended QM/MM zeolite models 5/240T and 11/83T, Section S3. The 240T cluster, including a 5T QM region, comprises 768 atoms in total with a full supercage surrounded by 10 sodalite cages. We optimized the geometry of the above mentioned six key structures using those extended models 5/240T and 11/83T. The same computational protocol as used for the (original) 5/83T model was applied, optimization with PBE/6-31G(d,p) and refine the energetics with PBE/6-311++G(2d,p), see Computational details of the main text.

Functionals. To evaluate the effect of varying the functionals on the observed energy difference between the crucial barriers, we carried out single-point calculations applying the hybrid functionals B3LYP and M06 to the same six key structures, invoking geometries optimized with the 5/83T model and the PBE/6-31G(d,p) functional.

Reaction energetics. Our results shows that both extended zeolite models 5/240T and 11/83T result in an increased difference, of 27–29 kJ mol^{-1}, between the crucial barriers of variants **MC2** and **MC3**, Table S4. Similarly, the tests using the functionals B3LYP or M06 increased the barrier difference, to 48 kJ mol^{-1} and 29 kJ mol^{-1}, respectively, Table S4. Overall, our test calculations suggest that pathway **MC3** is less favorable than pathway **MC2**, thus not operative for the formation of butene.

Table S4. Absolute reaction and activation free energies ΔG_{abs} (kJ mol^{-1}) of the key structures for pathways **MC2** and **MC3** with respect to complex **24,** $[Rh(C_2H_4)_3]^+$, using extended QM/MM models and functionals B3LYP or M06.

Complex	ΔG_{abs}			
	11/83T	5/240T	B3LYP	M06
24	0	0	0	0
35	-13	-15	-4	5
37	24	15	17	33
37_38	46	41	36	57
42	27	21	28	38
42_43	73	70	84	86

Section S10. Sketches of intermediates and transition states

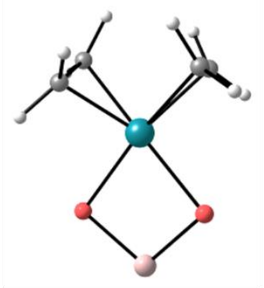

1

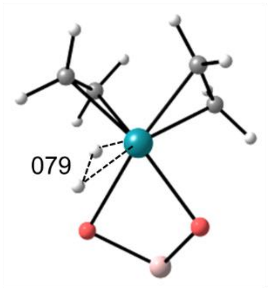

2

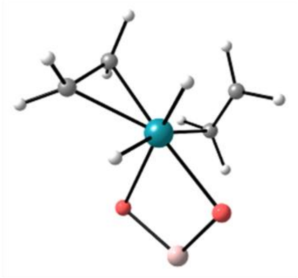

3

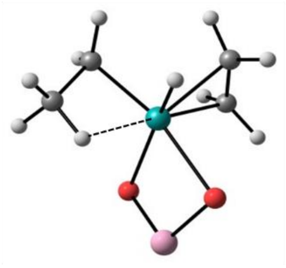

4

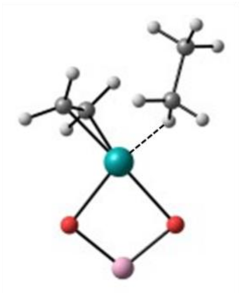

5

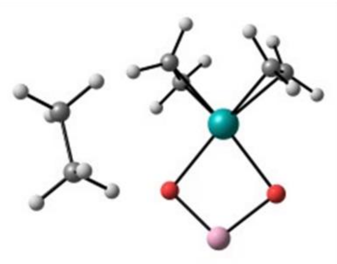

6

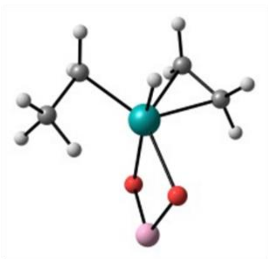

7

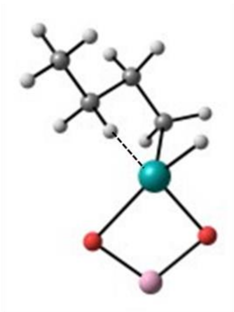

8

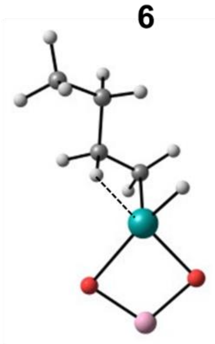

9

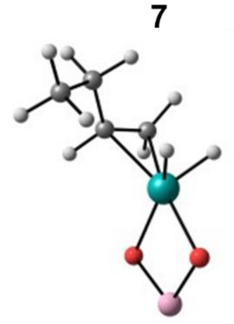

10

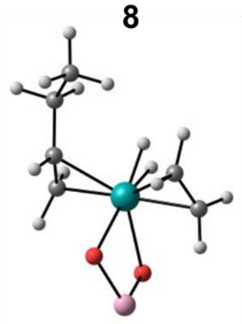

11

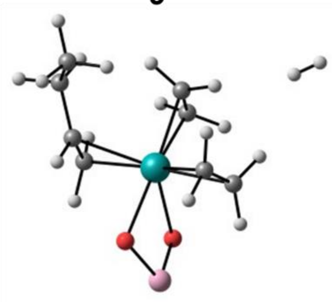

12

Figure S8. Optimized structures of intermediates involved in the ethene conversion mechanism, hydrogenation or dimerization, for zeolite-supported Rh(I) complex **1**, $[Rh(C_2H_4)_2]^+$, according to 2-ligand and 3-ligand based models. For clarity, only the structures of the active site are shown. Selected distances in pm.

Figure S8 (continued)

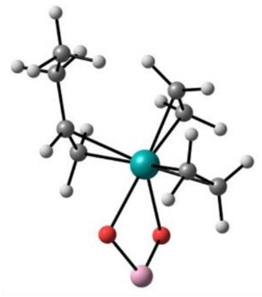

13

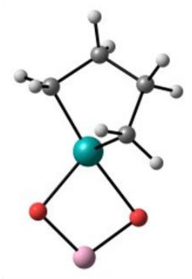

14

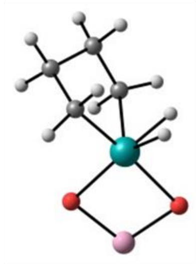

15

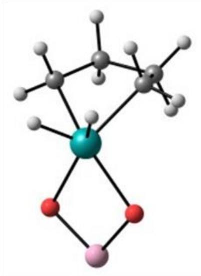

16

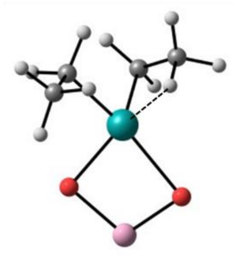

17

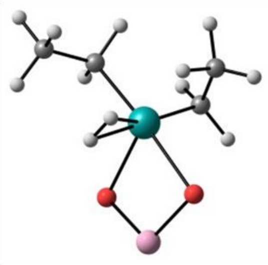

18

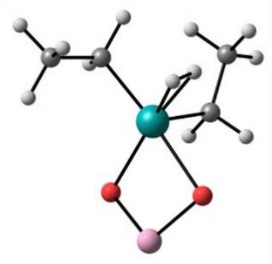

19

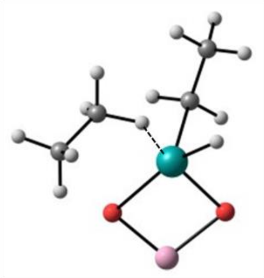

20

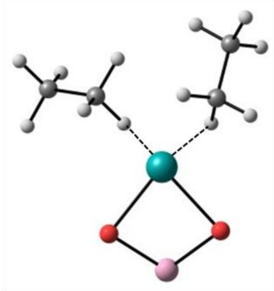

21

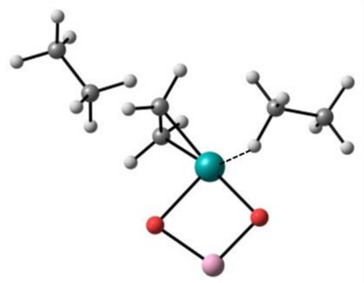

22

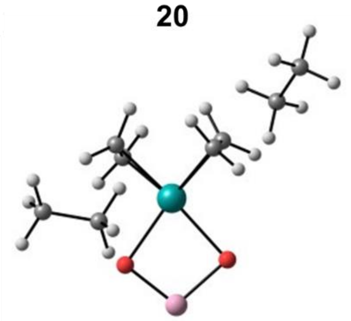

23

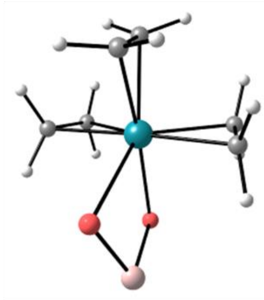

24

Figure S8 (continued)

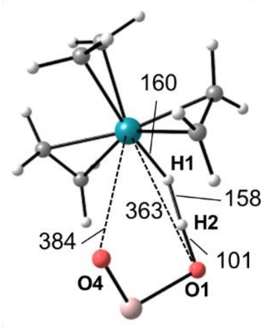

25

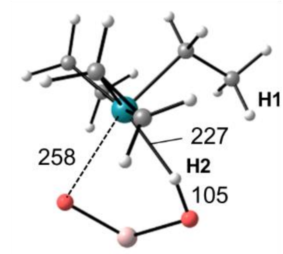

26

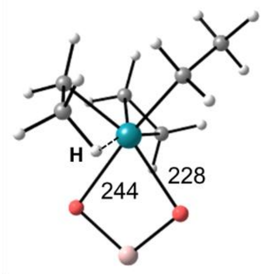

27

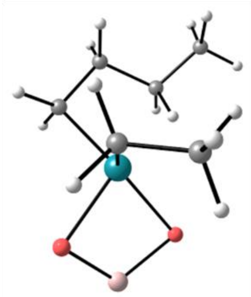

28

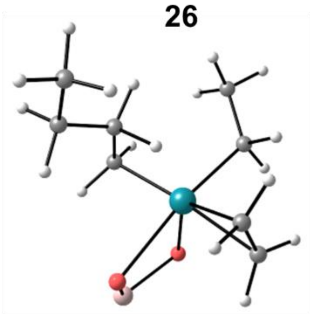

29

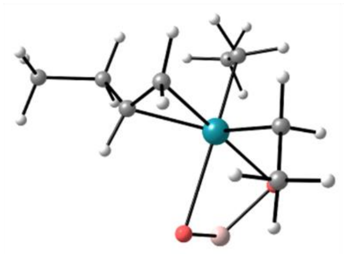

30

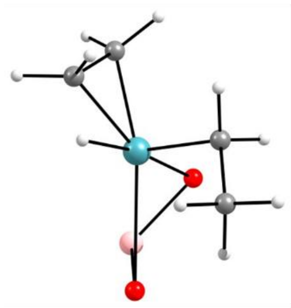

31

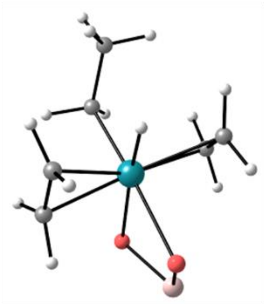

32

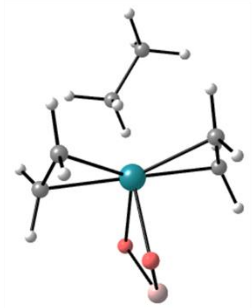

33

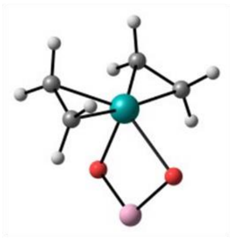

34

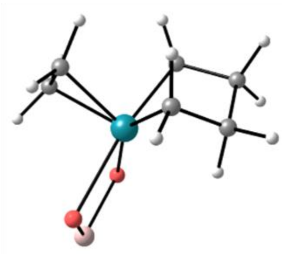

35

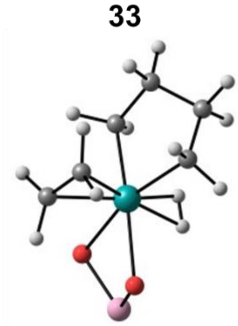

36

Figure S8 (continued)

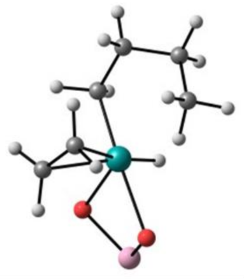

37

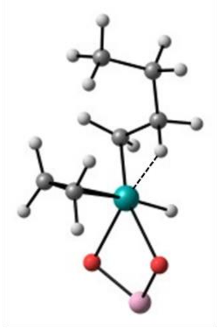

38

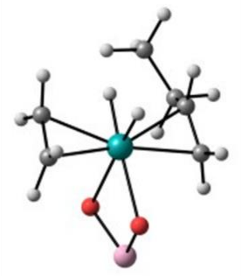

39

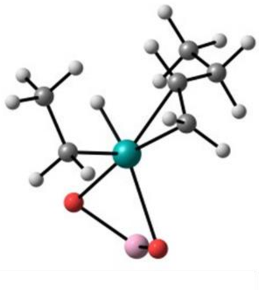

40

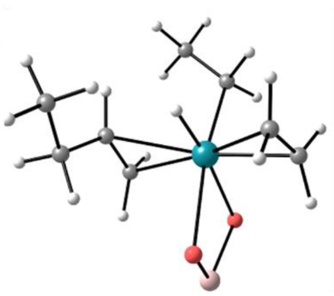

41

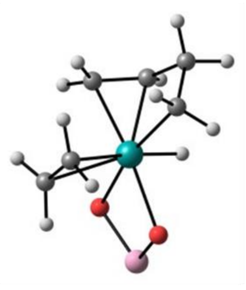

42

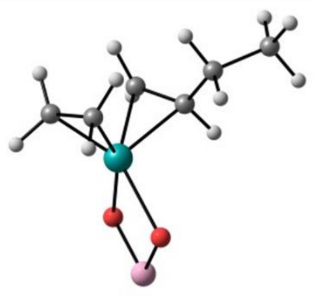

43

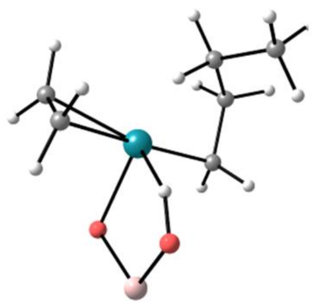

44

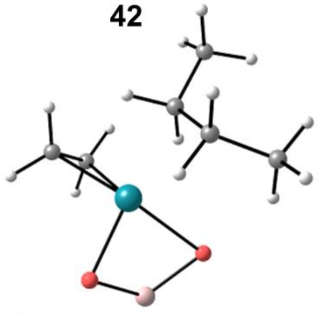

45

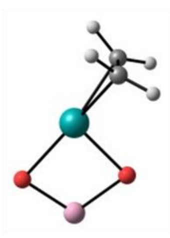

46

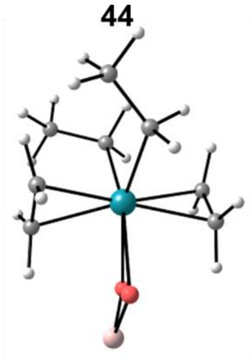

47

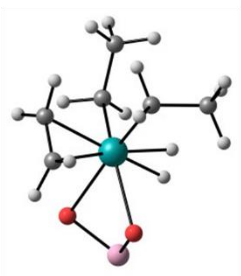

48

Figure S8 (continued)

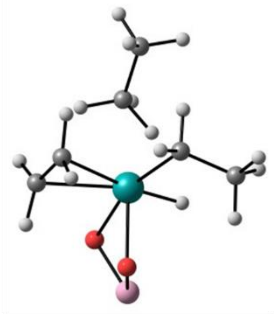

49

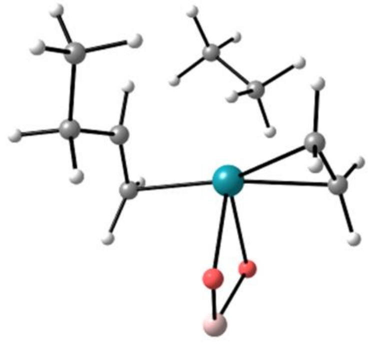

50

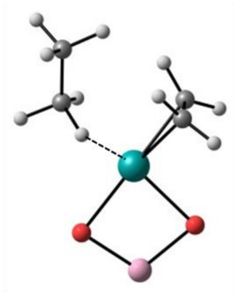

51

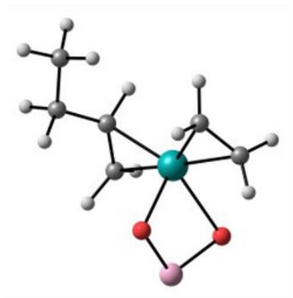

52

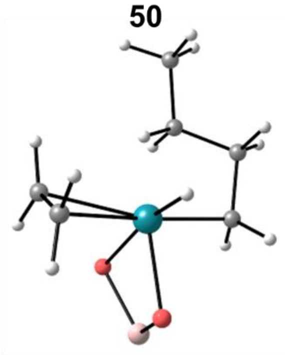

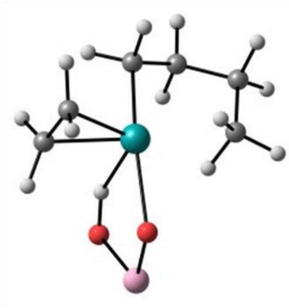

54

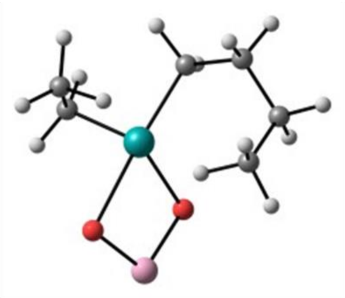

55

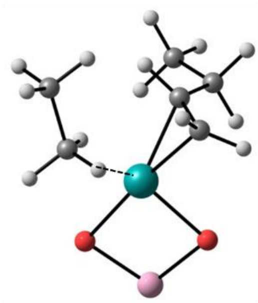

56

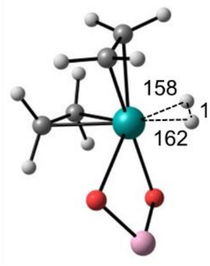

2_3

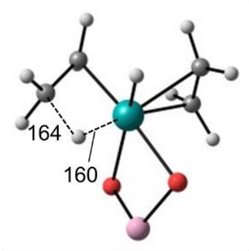

3_4

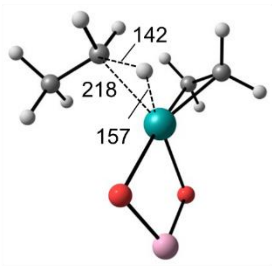

4_5

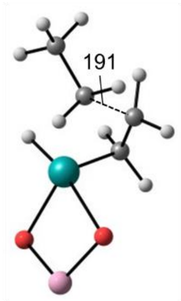

7_8

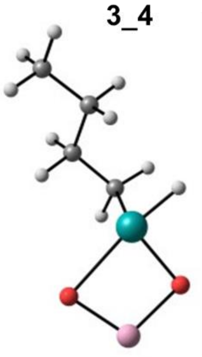
8_9

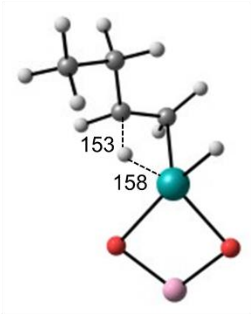

9_10

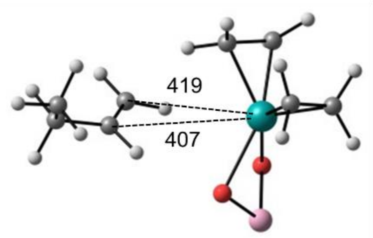

13_1

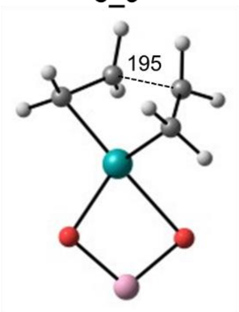

1_14

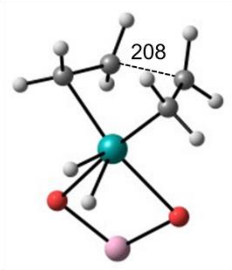

2_15

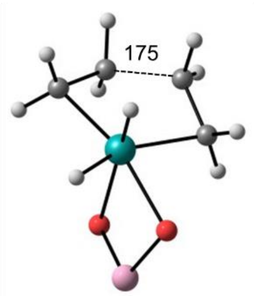

3_16

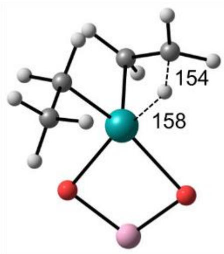

4_17

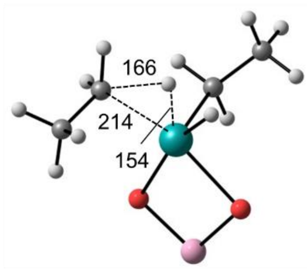

19_20

Figure S9. Optimized structures of transition states involved in the ethene conversion mechanism, hydrogenation and dimerization, for zeolite-supported Rh(I) complex **1**, $[Rh(C_2H_4)_2]^+$, according to 2-ligand and 3-ligand based models. For clarity, only the structures of the active site are shown. Selected distances in pm.

Figure S9 (continued)

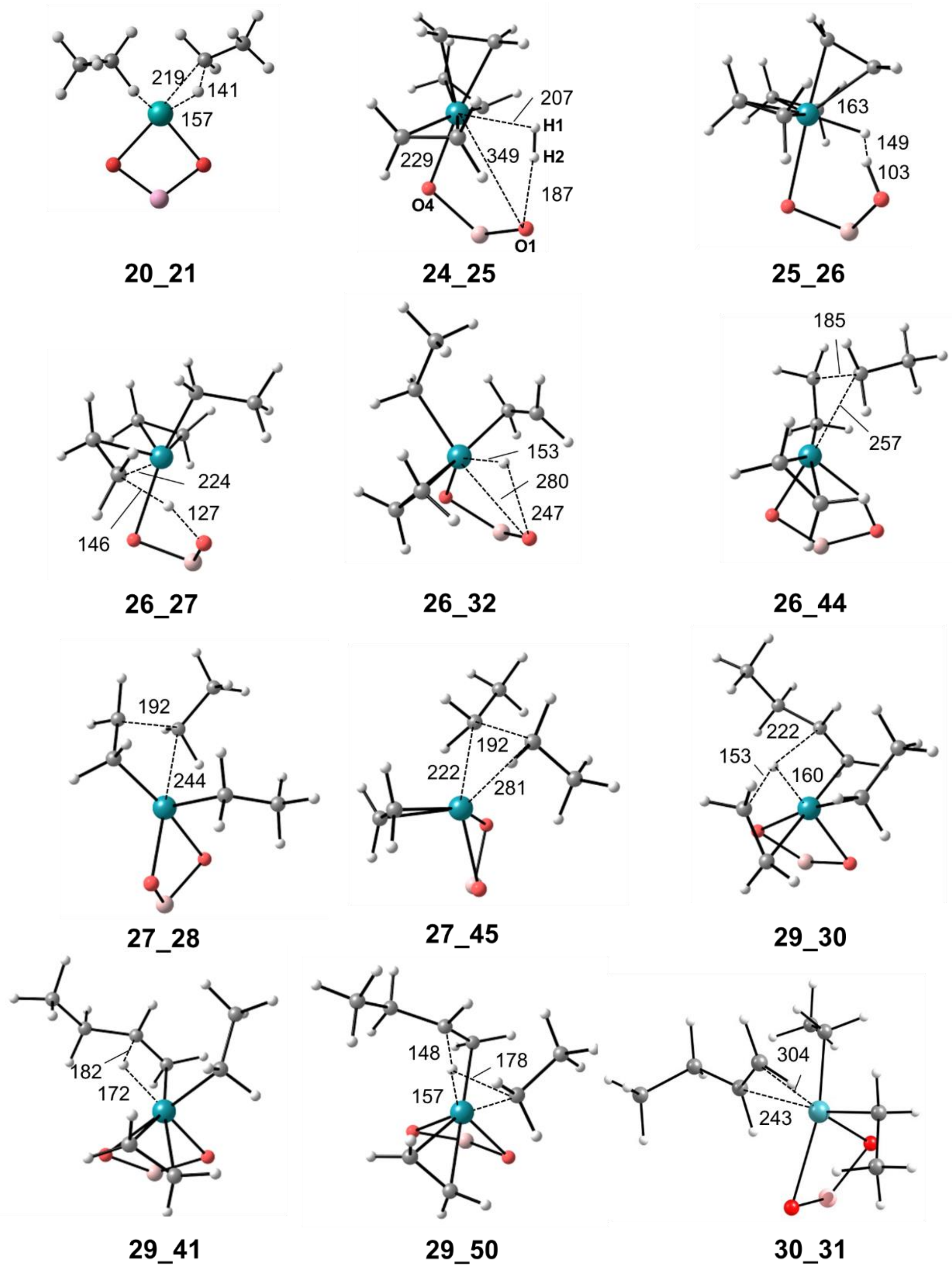

Figure S9 (continued)

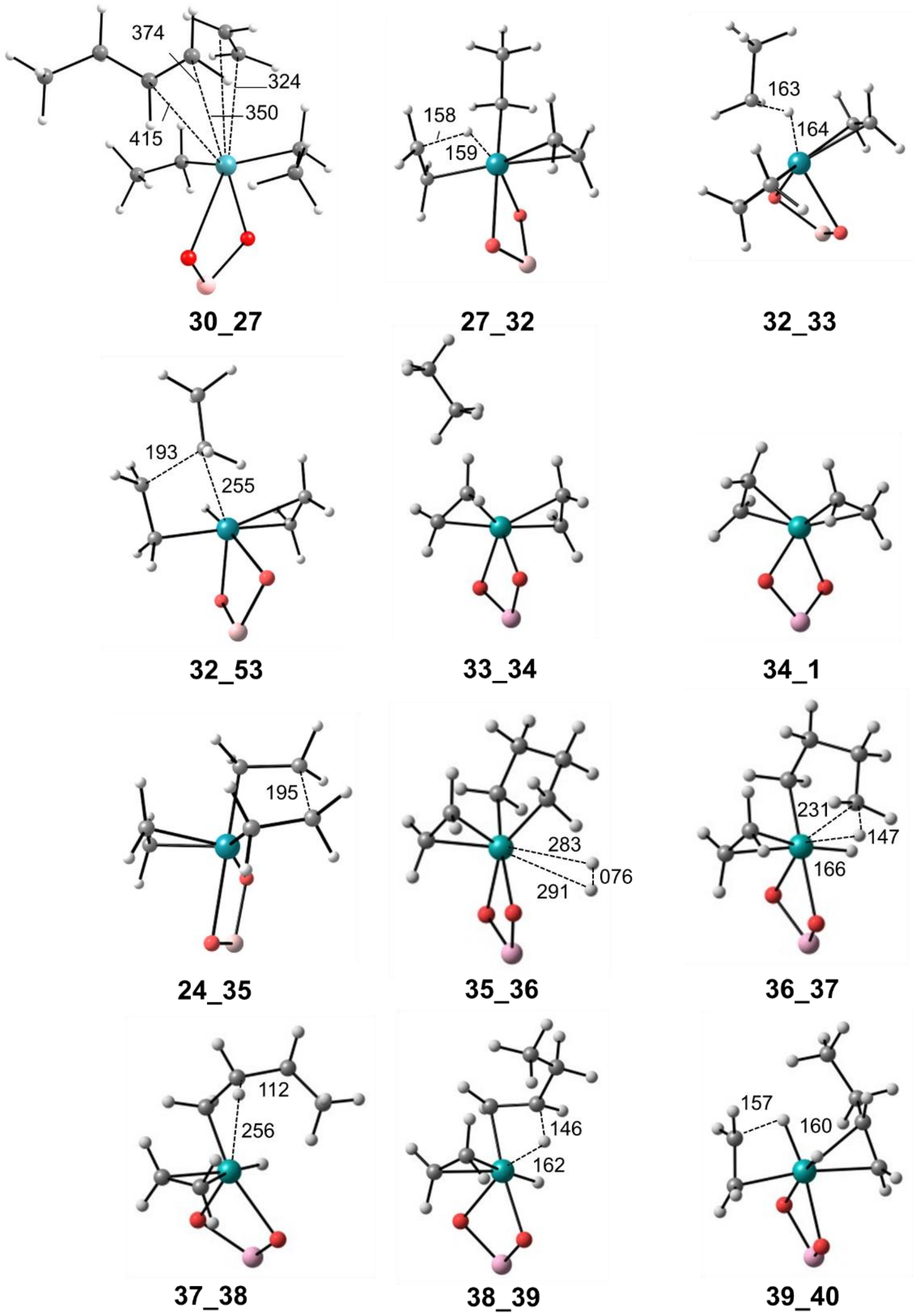

Figure S9 (continued)

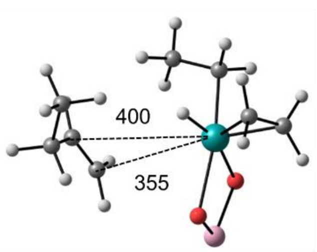

41_4

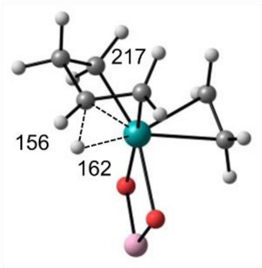

35_42

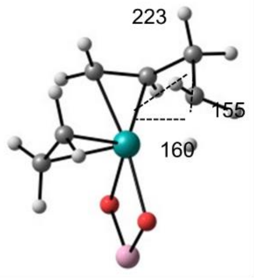

42_43

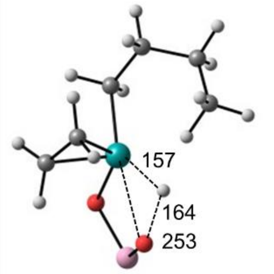

37_54

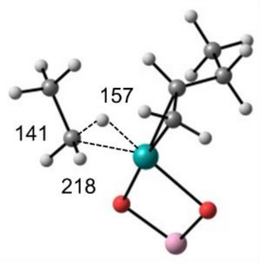

40_56

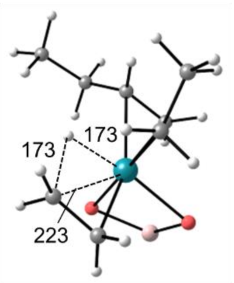

41_30

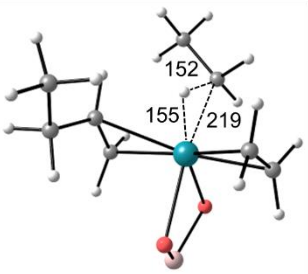

41_50

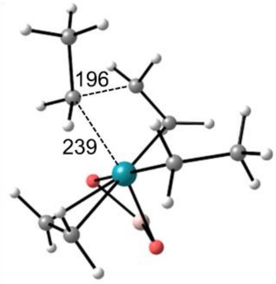

47_29

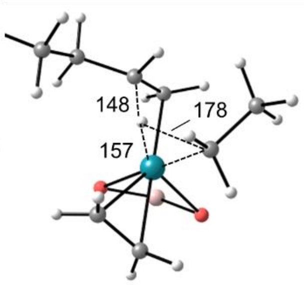

48_49

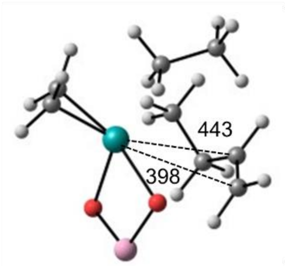

50_51

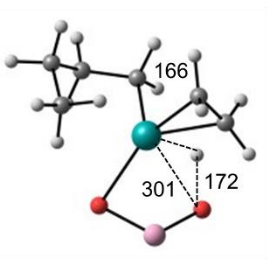

54_55

References

1. P. Serna and B. C. Gates, *Angew. Chem. Int. Ed.*, 2011, **50**, 5528-5531.
2. P. Serna and B. C. Gates, *J. Am. Chem. Soc.*, 2011, **133**, 4714-4717.
3. W. Loewenstein, *Am. Mineral.*, 1954, **39**, 92-96.
4. J. Dědeček, , Z. Sobalik, B. Wichterlova, *Catal. Rev. - Sci. Eng.*, 2012, **54**, 135-223.
5. A. Govindasamy, V. K. Markova, A. Genest and N. Rösch, *Catal. Sci. Technol.*, 2017, **7**, 102-113.
6. S. Dinda, A. Govindasamy, A. Genest and N. Rösch, *J. Phys. Chem. C*, 2014, **118**, 25077-25088.
7. S. H. Vosko, L. Wilk and M. Nusair, *Can. J. Phys.*, 1980, **58**, 1200-1211.
8. C. Lee, W. Yang and R. G. Parr, *Phys. Rev. B*, 1988, **37**, 785-789.
9. A. D. Becke, *J. Chem. Phys*, 1993, **98**, 5648-5652.
10. P. J. Stephens, F. J. Devlin, C. F. Chabalowski and M. J. Frisch, *J. Phys. Chem.*, 1994, **98**, 11623-11627.
11. Y. Zhao and D. G. Truhlar, *Theor. Chem. Acc.*, 2008, **120**, 215-241.